NanoTopoChip

Acta Biomaterialia 62 (2017) 188–198

Contents lists available at ScienceDirect

Acta Biomaterialia

journal homepage: www.elsevier.com/locate/actabiomat

Full length article

NanoTopoChip: High-throughput nanotopographical cell instruction

Frits F.B. Hulshof [a,b], Yiping Zhao [c], Aliaksei Vasilevich [b], Nick R.M. Beijer [b], Meint de Boer [d], Bernke J. Papenburg [c], Clemens van Blitterswijk [e], Dimitrios Stamatialis [a], Jan de Boer [b,*]

[a] MIRA Institute for Biomedical Technology and Technical Medicine, (Bio)artificial Organs, Department of Biomaterials Science and Technology, University of Twente, Enschede, The Netherlands
[b] MERLN Institute for Technology-Inspired Regenerative Medicine, Department of Cell Biology-inspired Tissue Engineering, Maastricht, The Netherlands
[c] Materiomics BV, Maastricht, The Netherlands
[d] MESA+Institute for Nanotechnology, University of Twente, Enschede, The Netherlands
[e] MERLN Institute for Technology-Inspired Regenerative Medicine, Department of Complex Tissue Regeneration, University of Maastricht, Maastricht, The Netherlands

ARTICLE INFO

Article history:
Received 14 February 2017
Received in revised form 8 August 2017
Accepted 16 August 2017
Available online 18 August 2017

Keywords:
Nanotopography
High-content imaging
Computational modelling

ABSTRACT

Surface topography is able to influence cell phenotype in numerous ways and offers opportunities to manipulate cells and tissues. In this work, we develop the Nano-TopoChip and study the cell instructive effects of nanoscale topographies. A combination of deep UV projection lithography and conventional lithography was used to fabricate a library of more than 1200 different defined nanotopographies. To illustrate the cell instructive effects of nanotopography, actin-RFP labeled U2OS osteosarcoma cells were cultured and imaged on the Nano-TopoChip. Automated image analysis shows that of many cell morphological parameters, cell spreading, cell orientation and actin morphology are mostly affected by the nanotopographies. Additionally, by using modeling, the changes of cell morphological parameters could by predicted by several feature shape parameters such as lateral size and spacing.

This work overcomes the technological challenges of fabricating high quality defined nanoscale features on unprecedented large surface areas of a material relevant for tissue culture such as PS and the screening system is able to infer nanotopography – cell morphological parameter relationships. Our screening platform provides opportunities to identify and study the effect of nanotopography with beneficial properties for the culture of various cell types.

Statement of Significance

The nanotopography of biomaterial surfaces can be modified to influence adhering cells with the aim to improve the performance of medical implants and tissue culture substrates. However, the necessary knowledge of the underlying mechanisms remains incomplete. One reason for this is the limited availability of high-resolution nanotopographies on relevant biomaterials, suitable to conduct systematic biological studies. The present study shows the fabrication of a library of nano-sized surface topographies with high fidelity. The potential of this library, called the 'NanoTopoChip' is shown in a proof of principle HTS study which demonstrates how cells are affected by nanotopographies. The large dataset, acquired by quantitative high-content imaging, allowed us to use predictive modeling to describe how feature dimensions affect cell morphology.

1. Introduction

Cells are known to respond to topographical cues of the substrate they come into contact with. Therefore, design of surface topography can be a strategy to influence the response of cells and tissues to biomaterials. Understanding the underlying mechanisms of cell-topography interactions and applying them for biomaterial design is valuable not only to improve *in vitro* culture systems [1] but also to improve the interaction of biomedical devices with the human body [2]. Microscale topography can strongly affect cellular and nuclear morphology. It can have a strong effect on cell adhesion, the organization of the (nucleo)cytoskeletal system and on fundamental aspects of cell physiology such as differentiation, proliferation, pluripotency and motility [3]. Nanoscale topographies are in the size range of filopodia, focal adhesions, lipid rafts,

* Corresponding author.
E-mail address: jan.deboer@maastrichtuniversity.nl (J. de Boer).

http://dx.doi.org/10.1016/j.actbio.2017.08.023
1742-7061/

endocytic vesicles and extracellular matrix fibers and may thus affect very different molecular mechanisms than microscale topographies. Molecular events affected are the spacing and clustering of transmembrane adhesion proteins such as integrins that are part of focal adhesion signaling complexes [4,5]. This is also supported by the fact that nanotopography affects downstream signaling events such as activation of the integrin-linked kinase/β-catenin pathway [6]. Cells are aligned through the spacing and alignment of focal adhesions by nanoscale wrinkled surfaces [7]. Further downstream, nanotopographies affect cell migration [8], proliferation [9] and differentiation [10,11]. Additionally, nanotopography can enhance extracellular matrix (ECM) production [12] and may also affect the ECM architecture. Furthermore, there are strong indications that nanotopography plays a role *in vivo*, for example: the surface structure of the basement membrane that interacts with epithelial cell layers [13].

The ability of exact shape design offered by lithographic techniques provides a more precise control over the dimensions of microscale topographies in comparison to non-lithographic techniques such as sand blasting, acid etching [14] and polymer phase separation [15]. Although this exact control over the dimensions of the surface topography improved the manipulation of aspects of cell morphology, the correlation between cell shape and cell phenotype is largely unknown. Therefore we and others have employed screening approaches to learn about the relationship between topographical design and cellular response [16,17]. We previously created the TopoChip high throughput screening platform [18], which allows simultaneous screening of thousands of randomly generated microtopographies. This "micro-TopoChip" contains topographies with height of 10 μm and lateral dimensions that range between 5 μm and 30 μm. We have shown that these topographies have significant effects on hMSC differentiation [18] and can maintain pluripotency of induced pluripotent stem cells [1]. Additionally the screening systems can be used to infer topography design – cell morphology/differentiation relationships [19].

In this work we aim to expand the high-throughput screening system with designed nanoscale topographies, which allows investigation of a library of nanoscale topographies and to tap into a new array of cellular mechanisms to influence cell fate. Systematic investigation of cell response requires larger substrate areas to be able to measure enough cells to perform statistical analyzes on subtle changes. To fabricate such nanotopographies for biological studies, high resolution beam writing techniques such as e-beam or ion-beam lithography are often used, because standard photolithography cannot reach the required resolutions. However, compared to lithography, beam writing has long writing times covering large areas of multiple cm^2, which lowers throughput. This severely limits the realistic area size, which can be patterned by these techniques. Advanced lithographic techniques such as Deep UV (DUV) and extreme UV (EUV) lithography are more suitable for the nanopatterning of large areas. While these techniques are being employed in the semi-conductor industry, they are usually not easily accessible by academic institutions due to their complexity and resulting high cost [20]. Here, to create the Nano-TopoChip, we use conventional UV lithography and DUV lithography in combination with a custom designed DRIE process to fabricate moulds for nano imprint lithography (NIL). Its design is made by computational pattern generation similar to the micro-TopoChip generation algorithm [18]. After successful production of the Nano-TopoChip, we first compare the effects of micro and nanotopography on U2OS osteosarcoma cells. Subsequently we use bioinformatics tools to identify which cell morphological parameters are affected by the nanotopographies. Finally, the links between surface topography design and cell morphological parameters are investigated by predictive modeling to understand how feature dimensions affect cell morphology.

2. Materials and methods

2.1. Nano-TopoChip design

Similar to the design of the micro-TopoChip [18], a custom C++ script is used to randomly select 1246 unique topographies from an *in silico* library of with a theoretical design space of millions of topographies that was generated by combining the primitive shapes triangle, rectangle and circle. A feature was generated by first randomly selecting parameter values for its size, the number of primitives to be used and the distribution over the different primitive types, the size of the primitives, and the degree to which the primitives were to be aligned. The parameter values were selected within the ranges that are shown in the Supplemental Table S1. Next, each primitive was placed at a random position inside the feature. Overlapping of primitives was also allowed. This random combination of the geometrical characteristics of the primitive shapes, such as sharp corners from triangles and rounded edges from circles, theoretically allows the generation of any shape. The script creates a Clewin image file, which was applied on a photomask. The resulting Nano-TopoChip contains a surface of 20 × 20 mm with 1246 unique topography designs *in duplo* in individual test surfaces of 390 by 390 μm called TopoUnits, each separated by 30 μm high, 10 μm wide walls in a 50 by 50 grid. The nano features within each TopoUnit are comprised of primitives of lines, circles and triangles have minimum and maximum lateral dimensions of 200 nm and 700 nm. Nano features with random shapes are generated with lateral dimensions ranging from 200 nm to 1000 nm.

2.2. Nano-TopoChip silicon master-mould fabrication

Supplementary Fig. 1 illustrates the Silicon Nano TopoChip fabrication process. Due to the difference of wafer size compatibility between different lithography instruments, the 76 mm diameter Si wafers were attached to the 100 mm diameter Si wafers using Fomblin oil during plasma etching processes. Double side polished, ⟨1 0 0⟩ oriented, 76 mm diameter Si wafers were used as obtained (Suppl. Fig. 1a). A bottom anti reflective coating (BARC) layer of 38 nm, a DUV resist layer of 225 nm, and a top anti reflective coating (TARC) layer of 90 nm were subsequently spin-coated and baked on the Si wafers (Suppl. Fig. 1b). The exposure was performed by an ASML PAS5500/1100B 100 nm ArF scanner using the conventional exposure mode. After exposure, the resist layer was developed and the TARC layer was removed during development. Detailed information about lithography materials, wafer preparation and exposure settings are proprietary information of ASML (Suppl. Fig. 1c). Next, the BARC layer was etched using mixed directional ion etching (DRIE, Alcatel AMS100SE Deep RIE system) by CHF_3 and Ar flow of 50 sccm respectively, automatic pressure control (APC) of 100%, inductively coupled plasma (ICP) power of 700 W, capacitively coupled plasma (CCP) power of 20 W with pulsed low frequency of 80/20 (on/off) ms and electrode temperature of −20°C. The etch rate of BARC was approximately 60 nm/min, and therefore the 38 nm BARC was removed in 45 s (Suppl. Fig. 1d). Si etching was performed using a nano Bosch DRIE (Alcatel AMS100SE Deep RIE system) by SF_6 (etching) and C_4F_8 (passivation) flow of 50 sccm respectively and cycle times of 1.5 s and 0.5 s respectively. Other settings were kept the same for both gases: APC of 100% ICP power of 1000 W, CCP power of 30 W with pulsed low frequency of 10/90 (on/off) ms and electrode temperature of −40 °C. The etch rates of silicon and resist are approximately 200 nm/min and 50 nm/min respectively (Suppl. Fig. 1e). Resist and BARC layers are stripped in O_2 plasma (Tepla 300), followed by Piranha cleaning for 15 min (H_2SO_4:H_2O_2 = 3:1, v/v,

96 °C). A fluorocarbon (CF) removal step was performed by first dry oxidizing the wafers at 800°C for 30 min followed by oxide removal in 50% HF for 1 min (Suppl. Fig. 1f). After standard cleaning (fumic HNO_3) for 10 min, and 69% HNO_3 at 96 °C for 10 min and native oxide removal 1% HF for 1 min), the wafers were prepared with 600 nm low pressure chemical vapor deposition (LPCVD) TEOS (silicon oxide formed by decomposing TetraEthylOrthoSilicate) followed by annealing at 1150°C in nitrogen environment for 3 h (Suppl. Fig. 1g). Adhesion promoter Hexamethyldisilane (HMDS) (Merck) and positive photo resist Olin 908-12 (Arch Chemicals) was spin-coated on the wafers (Suppl. Fig. 1h). A chromium mask, created by laser beam pattern generation with a Heidelberg DWL 200, containing 400 μm × 400 μm grids of 10 μm wide was used and the exposure was performed using conventional UV lithography (EVG 620) (Suppl. Fig. 1i). Pattern transfer from photoresist to annealed TEOS layer was performed by mixed DRIE (Alcatel AMS100DE Deep RIE system) using C_4F_8, He and CH_4 flow of 20 sccm, 150 sccm and 15 sccm respectively, pressure of 8.5 mbar, ICP power of 2800 W, CCP power of 350 W and electrode temperature of −10 °C. The etch rates of the annealed TEOS and photoresist were approximately 500 nm/min and 50 nm/min respectively (Suppl. Fig. 1j). After photoresist removal using O_2 plasma and Piranha cleaning (as described in step 6), silicon grids were etched using Alcatel AMS100 SE Deep RIE system by SF_6 and O_2 flow of 100 sccm and 40 sccm respectively, ICP power of 1000 W, CCP of 20 W with pulsed low frequency of 20/80 (on/off) ms and electrode temperature of −110°C (Suppl. Fig. 1k). The etch rates of Si was approximately 4.5 μm/min. In the final step, the annealed TEOS layer was removed by etching in 50% HF for 1 min (Suppl. Fig. 1l).

2.3. Ormostamp® mould fabrication

Supplementary Fig. 2 depicts the method to fabricate the OrmoStamp® mould. The silicon master mould was replicated into Ormostamp moulds in two replication steps. OrmoStamp® (Micro Resist Technology GmbH, Germany) is a UV curable inorganic-organic hybrid polymer and OrmoPrime®08 (Micro Resist Technology GmbH, Germany) is the adhesion promoter for OrmoStamp®. Detailed information about these two polymers can be found in the manufacturer's processing protocols. Borofloat wafers (Borofloat® 33 from Schott) of 100mm diameter and 500μm thickness were used. After Piranha cleaning and dehydration baking on a hot plate at 120 °C for a minimum of 10 min, OrmoPrime®08 was spin-coated on the Borofloat wafer at 4000 rpm for 30 s and then baked on a hot plate at 150 °C for 5 min. In our experiments, a Borofloat wafer with OrmoPrime®08 was prepared right before the application of OrmoStamp® (Suppl. Fig. 2a). A droplet of 1.5mL OrmoStamp® was slowly dispensed on the Si master mould and was slowly brought into contact with the Borofloat wafer with OrmoPrime®08 coating. Slow spreading of the droplet between the Borofloat wafer and Si mould was required to avoid air bubbles getting trapped (Suppl. Fig. 2b). The gap between the two substrates was completely filled by capillary force, which takes about 15–30 min. (Suppl. Fig. 2c). The Si and Borofloat wafer stack was exposed to 350–450 nm UV light for 90 s with the light intensity set at 12 W/cm^2 (EVG 620 i-line exposure system) (Suppl. Fig. 2d). The Si mould could easily be peeled off from the OrmoStamp® mould, after which the OrmoStamp® mould immediately followed a hard bake process at 130 °C on a hot plate (ramping up from 20 °C to 130 °C with a ramping speed of 5 °C/min). After hard baking for 30 min at 130 °C, this negative OrmoStamp® mould was cooled down together with the hot plate to room temperature (Suppl. Fig. 2e). Before the second replication step, the OrmoStamp® mould received a gentle O^2 plasma treatment by reactive ion etching (RIE, home-build) at 10 °C, 50 sccm O^2 flow, 75 mTorr pressure, and 50W CCP power for 30 s. After this a monolayer of fluoroctatrichlorosilane (FOTS) was deposited from gas phase under vacuum condition in a desiccator. For the second replication step another borofloat wafer was coated with OrmoPrime®08 as described in 3b (Suppl. Fig. 2f). As before, a droplet of 1.5 mL OrmoStamp® was slowly dispensed on the negative OrmoStamp® mould and is slowly brought into contact with the Borofloat wafer with OrmoPrime®08 coating (Suppl. Fig. 2g). Again, the gap between the two substrates was filled by capillary force (Suppl. Fig. 2h). The wafer stack was exposed to UV light (Suppl. Fig. 7i) after which the negative OrmoStamp® mould could easily be peeled off from the positive OrmoStamp® mould, after hardbaking (Suppl. Fig. 2j).

2.4. Polymer Nano-TopoChip fabrication

To prepare the OrmoStamp® mould for hot embossing, a gentle O_2 plasma treatment was performed using reactive ion etching (RIE, home-build) at 10 °C, 50 sccm O^2 flow, 75 mTorr pressure, and 50W CCP power for 30 s. A monolayer of FOTS was deposited from gas phase under vacuum condition in a desiccator (Suppl. Fig. 2k). Commercially available bi-axially oriented PS films of 190 μm (Goodfellow, United Kingdom) were used for hot embossing. PS hot embossing process was performed using the Obducat Eitre®6 Nano Imprint Lithography system (Obducat, Sweden). The PS film and OrmoStamp® mould were brought into contact (Suppl. Fig. 2l)) and the hot embossing was performed at a temperature of 140 and a pressure of 10 bar for 5 min (Suppl. Fig. 2m). Finally, the PS film was separated from the OrmoStamp® mould at 90 °C (Suppl. Fig. 2n). The Nano-TopoChips were treated with a very mild oxygen plasma before cell culture (the SEM images of the Nano-TopoChip were made after this treatment to make sure the nanotopographies were still intact). The Ormostamp moulds® could be used 3 times for hot embossing after which a deterioration of feature and wall quality was observed.

2.5. SEM imaging

The moulds and Nano-TopoChips were imaged with a Zeiss Merlin HR-SEM. Because the images where taken at an angle of 45° and some of the features are circles, the height (vertical dimensions) of the pillars was inferred with a correction factor, instead of being measured from cross sections. The correction factor was calculated by dividing the number of pixels comprising the × dimension of a circular feature by number of pixels comprising the y dimension of a circular feature. The true height of the features could be calculated by multiplying the measured height (under an angle of 45°) by the correction factor (1.33) (Suppl. Fig. 3).

2.6. Cell culture and imaging

U2OS cells, stably expressing Lamin B1 BFP, αTubulin GFP and Actin RFP (U2OS LMNB1-TUBA1B-ACTB, Sigma-Alldrich) were cultured in McCoys medium (Sigma-Alldrich) with 10% FBS (Sigma-Alldrich), 100 U/ml penicillin and 100 g/ml streptomycin (Gibco). The cells were passaged according to manufacturer's protocol. In all experiments, medium was refreshed every two days. For the screening experiment, the cells were seeded at a density of 5000 cells/cm^2 on 6 Nano-TopoChips with a custom built seeding device. The device consists of a culture chamber that fits 2 Nano-TopoChips and creates a small space (500 μm height) on top of the TopoChips. The limited space immobilizes the cell suspension by capillary force to achieve homogenous cell seeding for 4 h after which the lid is removed to allow culture in a conventional volume of medium for adequate nutrient supply and gas exchange. After 3 days of culture, the cells were washed in phosphate buffered (PBS,

Sigma Aldrich) and fixated with 1% paraformaldehyde for 10 mins at 0 °C, followed by quenching with 50mM ammonium chloride (Sigma Aldrich). Next, the cells were washed with PBS and incubated with 1: 10,000 4′,6-Diamidino-2-phenylindole (Dapi, Life technologies) for 30 min. Finally the Nano-TopoChips were mounted on coverslips with Mowiol 4-88 (Sigma Aldrich) after washing with PBS twice. After sample drying the chips were imaged using a Hamamatsu Nanozoomer. A complete image was generated from every Nano-TopoChip, which were subsequently cut into smaller images from individual TopoUnits for each separate channel.

2.7. Data analysis

Prior to image analysis, flat-field correction and image normalization were performed as described previously [19]. Open source software Cell Profiler (CP) was used for the image analysis [21]. In order to perform the automated image analysis in CP, a robust pipeline able to recognize the different cell features was built. The Data analysis was performed using R, a programming language and software environment for statistical computing and graphics [22]. The potential mis-segmentation of cells was detected based on cell area and intensity of the nucleus. The cells were gated based on cell area and perimeter, after which the cells in the upper right quadrant were excluded from further analysis (Suppl. Fig. 4). To exclude imaging artifacts that could be mistakenly recognized as nuclei, the cells were gated based on nuclei mean and integrated intensity, after which the cells in the lower left quadrant were excluded from further analysis (Suppl. Fig. 5).

The cell features with the highest variation within the whole dataset where identified with a Kruskall-Wallis test. The Kruskall-Wallis test is a non-parametric rank based-based test, analogues to analysis of variance (ANOVA). cell morphology parameters (Fig. 4a). For cell profiler features we took the distance weighted median [23] across all cells in TopoUnit. For the selected descriptors a rank of surfaces was created based on the distance-weighted median calculated from the replicas. For the classification analysis, the top and bottom 100 surfaces were selected. Before training the model we used a recursive feature elimination step to identify features that were important to discriminate these 2 classes. To create the models we used 75% of the TopoUnits and the accuracy of the model was accessed on the remaining 25%. The models were trained with a 10 fold cross validation in the "caret" package [24]. The performance of the model was assessed by accuracy which is the match between predicted class and actual class and ROC curve.

3. Results

3.1. Fabrication of the Nano-TopoChip

The Nano-TopoChip design was created by computational pattern generation. It has an area of 20 mm by 20 mm and contains 2500 TopoUnits of 390 μm by 390 μm each, separated by 10 μm thick walls. The nanotopographies were defined using an ASML PAS5500/1100B of 100 nm ArF scanner while the wall features were defined by conventional UV lithography. Therefore, a reticle for DUV exposure and a mask for conventional UV lithography were designed. The nanotopographies within the TopoUnits are comprised of primitives of squares, triangles and circles. Considering the maximum resolution of the ASML PAS5500/1100B ArF scanner of 100 nm, the lateral dimension of the nanotopographies range from 200 nm to 1 μm. Four Nano-TopoChips with a row and column spacing of 2.4 mm and 2.6 mm, respectively, were scanned on the wafer during DUV exposure. Accordingly, for the walls, grids of 20 mm by 20 mm area in the mask for conventional UV lithography were designed sharing the same row and column spacing. Wafers with testing features were first fabricated to test the DRIE BARC and DRIE processes. High-resolution scanning electron microscopy (SEM) images of BARC layer before and after etching are shown in Fig. 1a and b.

The optimized etching processes (described in methods) were used to fabricate the Si mould which is the negative of the Nano-TopoChip. The mould contains the 30 μm deep trenches (Fig. 1c) to form the walls that will separate the TopoUnits and the nano-seized cavities (Fig. 1d) that will form the nanotopographies. The clearly defined feature shapes are recognizable in the cavities. The silicon moulds were replicated into OrmoStamp® moulds with a two-step process described in the methods section. In summary the silicon mould is first replicated in first (positive) OrmoStamp® (Fig. 1e) which is subsequently replicated into a second (negative) Ormostamp (Fig. 1f). OrmoStamp® moulds enable hot-embossing of polystyrene (PS) films to create PS Nano-TopoChips. To demonstrate differences in dimensions between the features on the micro-TopoChip and the Nano-TopoChip an image of the micro-TopoChip (Fig. 1g) is shown below the image of the first Nano-TopoChip Ormostamp® mould (Fig. 1e) of the same magnification.

The second Ormostamp® mould was used to fabricate PS Nano-TopoChips by hot-embossing. SEM was used for quality inspection of several topographical features of the Nano-TopoChip (Fig. 2). The smallest pillars have lateral dimensions of 230 nm. The large features have lateral dimensions of up to 2 μm. The features have an average height of 750 nm (standard deviation of 68 nm). Due to the hot embossing process, the relatively smaller features are usually shorter (between 650 nm and 750 nm) while the relatively large features are taller (between 750 nm and 900 nm). We did not measure any significant differences in height of features within a TopoUnit (see Suppl. Fig. 6). Despite the high aspect ratio of features, for example the small pillars (Fig. 2cd), the features are stable and the replication is very good without having bending or breakage due to de-moulding. Sharp angles of the features (Fig. 2cd) are maintained through the replication process. The top of the features has nano-roughness similar to the non-patterned areas; this roughness is probably created by the mild oxygen plasma treatment of the Nano-TopoChips that is required for adequate cell adhesion to PS. In fact, complex defined shapes are produced with high quality and reproducibility at varying densities on relatively large surface areas. Therefore, we think that the Nano-TopoChip can set a new benchmark for resolution of topographies on a large biomaterial surface area, in comparison to state of the art topographies used for biomedical studies, [17,25–27].

3.2. The nano-TopoChip generates distinct U2OS cell morphologies in comparison to the (micro)TopoChip

To compare the effect of the topographies on cell morphology between the micro- and Nano-TopoChip, we first performed an experiment with the transgenic U2OS cell line, which stably expresses Actin-RFP, cultured on the micro-TopoChip (Fig. 3a). Similar to earlier observations using bone marrow-derived human mesenchymal stem cells [18], U2OS cells show a large variety of morphologies on the micro-TopoChip. The topographies mould the cells in various shapes and in some cases, align the cells into grids (Fig. 3a, image 2). In many cases the actin fibers are combined into thick bundles with a clear orientation directed by the topography (Fig. 3a, images 1,2,3). Noteworthy are the extreme nuclear morphologies (Fig. 3a, images 4,5) that are induced micro topographies. On the microtopographies a classic oval nuclear shape, common on standard culture plastics, is rarely encountered. In fact, the microtopographies induce strong bends in the nuclear membrane and in some cases the nucleus is forced around the features in thin curves shapes (Fig. 3a, image 4).

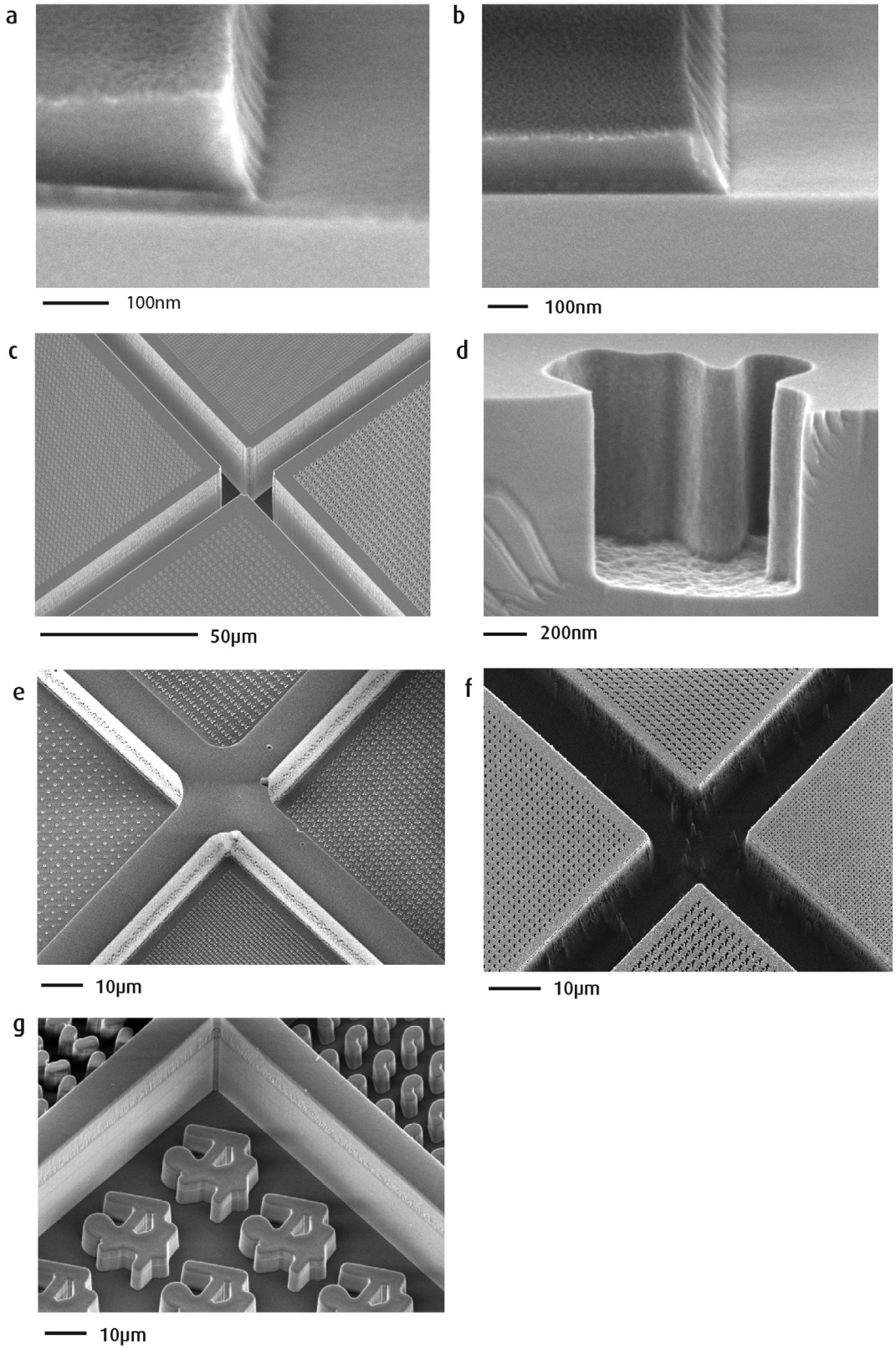

Fig. 1. Quality control of Nano-TopoChip mould fabrication steps a: SEM images of BARC layer before etching. b: SEM images of BARC layer after etching. SEM images of nano TopoChip fabrication result. c: A zoom-out image of a nano feature separated by 30 μm grid trenches. d: A zoom-in image of a nano feature with random contour and smooth bottom and sidewall profile. e: SEM images of the first (positive) Ormostamp mould. f: SEM images of the second (negative) Ormostamp mould used for hot-embossing of PS to create the Nano-TopoChips. g: SEM image of a Titanium coated micro-TopoChip for size comparison to the first (positive) Ormostamp® mould with the same magnification.

Next, to investigate the effect of nanotopography on cell morphology, U2OS cells were cultured on 6 Nano-TopoChips for three days. Visual inspection of the images shows that the nanotopographies also affect U2OS morphology in various ways and that those are distinctly different from the micro-TopoChip (Fig. 3b). On the Nano-TopoChip, we do not observe gross differences in cellular

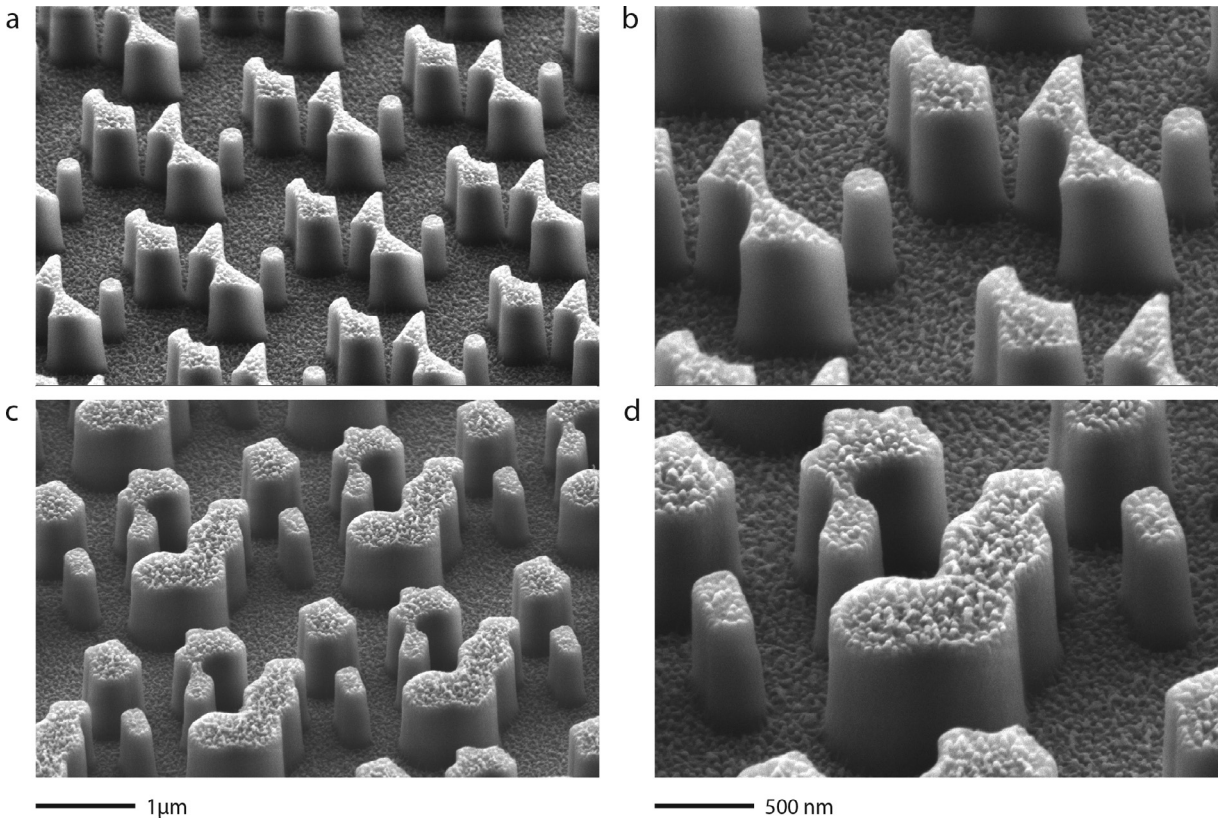

Fig. 2. Quality control of PS Nano-TopoChip. Two topographical features (a + b, c + d) were selected to demonstrate the fabrication quality of nanostructures that have various shapes and densities. b and d, are higher magnification images of topographies shown in a and c respectively.

shapes but the nanotopographies seem to affect the extent of cell spreading and the organization of the actin localization. On the nano features, the actin fibers align in various different orientations and patterns (Fig. 3b, images 1,2,3). Interestingly, some features induce the formation of a greater number and larger size filopodia (Fig. 3b, images 4,5), while other nano features create very fine actin distinctly spaced actin fibers (Fig. 3b 3,6). The more spread cells have very distinct punctate patterns of actin fibers (Fig. 3b, image 7), while the less spread cells tend to have more cortical actin (Fig. 3b, image 4). In this initial observation, the morphology of U2OS nuclei does not seem to deviate much from the common 'classic' oval shape (Fig. 3c).

3.3. The Nano-TopoChip is to infer nanotopography – cell morphology relationships

To quantify the morphological effects of the nanotopographies, we analyzed the images from the 6 Nano-TopoChips using a combination of bioinformatics tools. First, images in the dataset were filtered for outliers caused by events such as focus artifacts and dust particles by using a power log-log slope method (see methods), which might otherwise cause extreme mis-segmentation artifacts. The amount of cells per unit followed a normal distribution (see Suppl. Fig. 9) and a median of 24 cells were measured in every TopoUnit in the filtered dataset. Because a total of 6 Nano-TopoChips (which each contain the topographies *in duplo*) were used in the screening experiment, this resulted in more than 200 measured cells for every Topography. Next, the images were segmented and parameters (Suppl. Table 2) such as cell solidity, alignment, number, size and extent were measured by Cell profiler [21], resulting in a dataset for analysis containing 288 (including Metadata) features for each cell. In this experiment, more than 470 thousand cells were measured on a total of 15000 TopoUnits.

To identify the cell features with the highest variation within the whole dataset, a Kruskall-Wallis test was performed on the cell morphology parameters (Fig. 4a). In line with the visual observations the highest variation within the dataset is on parameters that determine cell area (Perimeter, Area, Axis Lengths, Diameter) and orientation (Orientation). When we performed the same test on nuclear morphology parameters, we noticed that only the orientation is affected by the topographies (Fig. 4b), whereas there is little effect on the nuclear morphology parameters such as shape and area. This is in line with our visual inspection, which showed that the nuclear morphology not affected by the nanotopographies, especially so when compared to the effect of microtopographies.

To confirm that we can screen for biologically meaningful parameters such as cell spreading, we also quantified the median cell area for every TopoUnit (Fig. 5a). The S-shaped curve shows that the cell area has a normal distribution with a minimum median size of 2460 μm^2 (17500 pixels) and a maximum median size of 4570 μm^2 (32500) pixels. The cells on the non-patterned TopoUnits (indicated by the blue dot) have a median size of 3234 μm^2 (23000 pixels), which is right in the middle of the distribution, showing that a non-patterned surface, on average, leads to a medium cell size. Representative images of small area cells and large area cells as quantified by Cell profiler is shown in Fig. 5b. The actin organization is very different between the large area and small area cells. The small area cells have a large amount densely aligned thin fibers, while the large cells have shorter, thicker fibers with isotropic orientations.

To assess if we can accurately predict cell size with surface design parameters, we selected top and bottom ranked surfaces based on cell area as was discussed before (1). We found that random forest was able to predict cell area most accurately (Fig. 5c). The area of the smallest individual structure, the 10th percentile of pillars size within the topography and the ratio between area

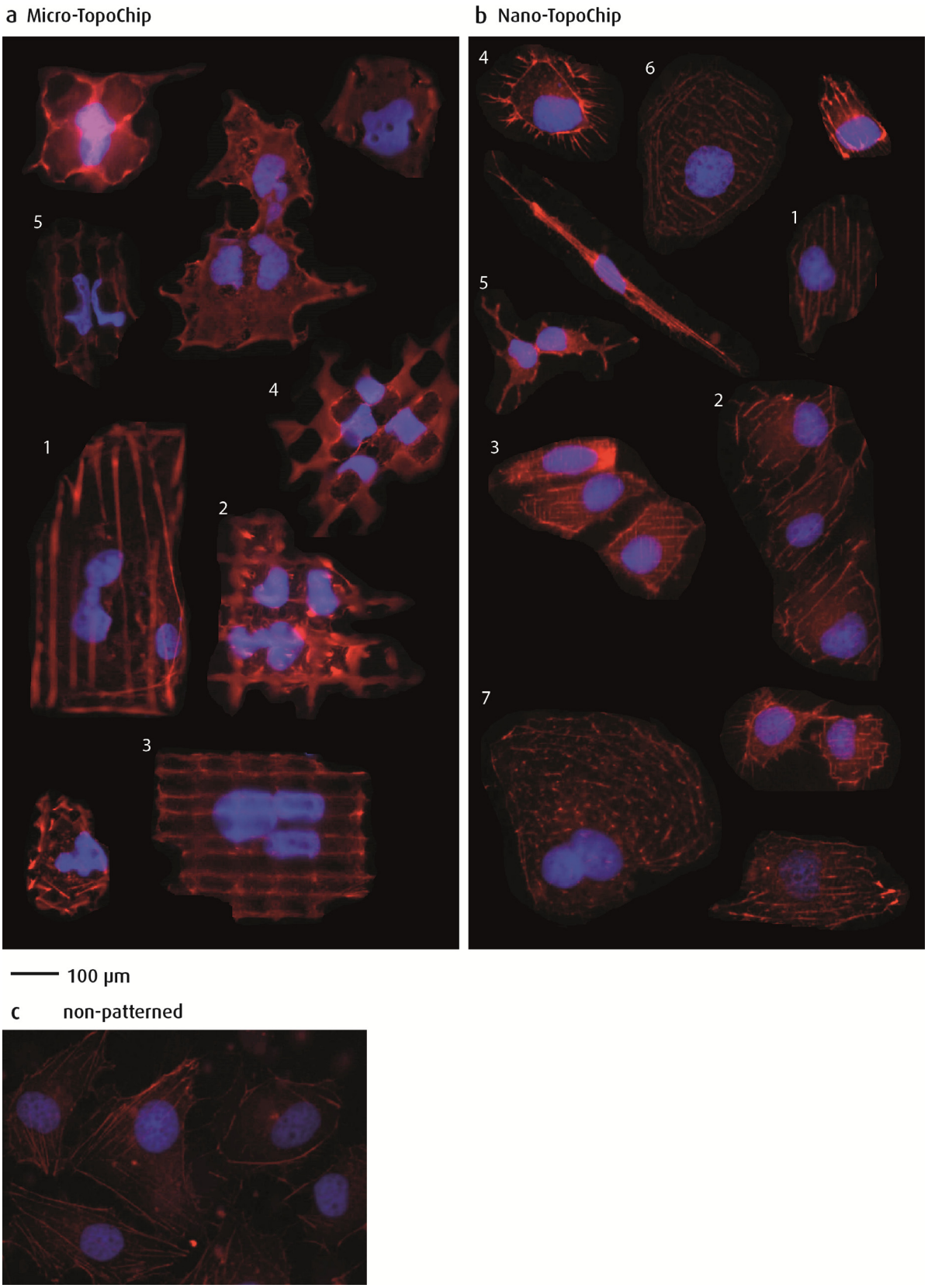

Fig. 3. U2OS Cell morphology on micro- and Nano-TopoChip a: Collage of U2OS cultured on the micro-TopoChip. b: Collage of U2OS cultured on the Nano-TopoChip. c: Image of U2OS cultured on non-patterned surface. Zoom-in images of these collages are shown in the Supplementary Figs. 7 and 8.

covered by topographical features and the area not covered by topographical features (pattern density) calculated by 2 methods were the most predictive parameters. These surface design parameters were able to predict cell size with 98% accuracy (Fig. 5d). Visual inspection of the topography designs confirms the model predictions (Fig. 5e). The topographies that induce small, more

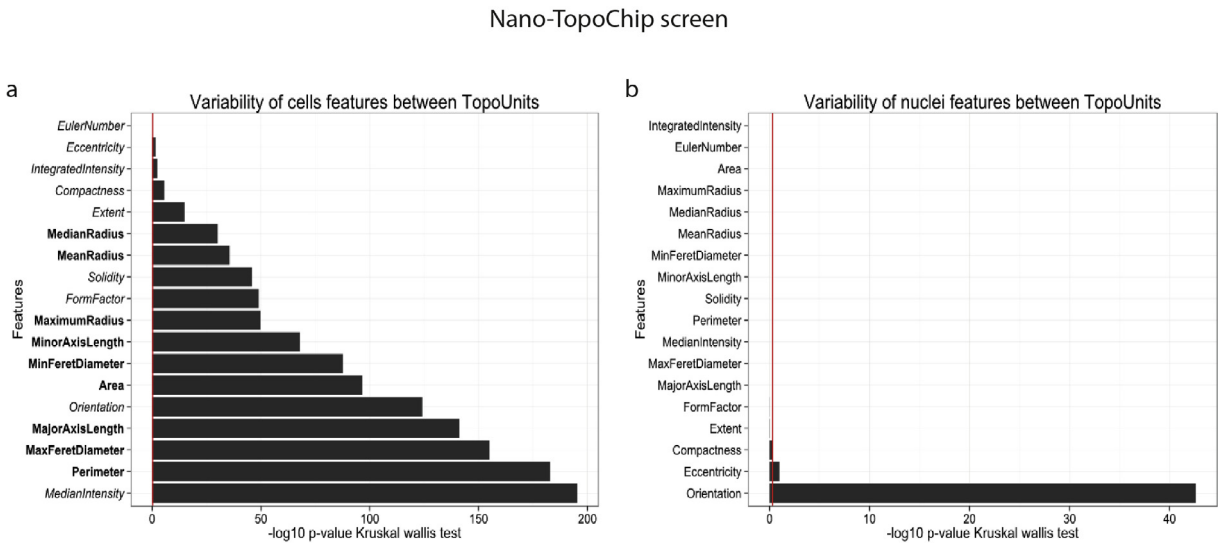

Fig. 4. Nanotopographies influence many cell morphological parameters a: Kruskall-wallis test to identify cell morphological parameters which show the most reproducible variation within the dataset. b: Kruskall-wallis test to identify nuclear morphological parameters which show the most reproducible variation within the dataset.

rounded cells, consist of relatively large topographies with large spacing between the topographies. The topographies which induce more spreading of the cells consist of smaller features which also cover a relatively small area. Other parameters such as cell number (Fig. 6a), actin localization (Fig. 6b) and fiber actin alignment (Fig. 6c) could also be predicted by feature design parameters, using the same methods.

4. Discussion

This work shows, for the first time, the fabrication of high quality designed nanometer scale features on a large area such as a 4 cm^2 on the Nano-TopoChip, using deep UV projection lithography in combination with conventional lithography [20]. Since large surface areas are required to accurately measure events in populations of cells the Nano-TopoChip is an important step towards development of a platform for HTS of events at this scale. In this work we fabricated the Nano-TopoChip in PS as it is the golden standard in tissue culture and provides excellent optical properties, which facilitate high-throughput image-based screening experiments. However, one of the major advantages of our fabrication method is that it can be produced in many other different (biomedical) polymers. Surface chemistry strongly dictates cell response [28–30] and may play a critical role in how cells respond to topography. A limitation of the fabrication method which relies on several hot-embossing steps is the introduction of variance in feature height between the small and large features. This is probably caused by imperfect filling of the cavities in the moulds which was unfortunately necessary to enable successful de-moulding of a hard and brittle material such as PS. It is possible to achieve a more uniform feature height by using softer biomaterial substrates.

Comparison of the influence of micro- and nanotopography on cell morphology yielded multiple important observations. The nanotopographies have a limited effect on nuclear morphology which can be extremely affected by micro topographies. The nanotopographies are not able to limit cell volume and shape by moulding the cells between the features such as is often the case with micro topographies. However, they are able to influence cell spreading and actin morphology. In stem cells subtle changes in actin morphology can be correlated to lineage fates [31]. By controlling actin morphology we might be able to steer stem cell differentiation.

The machine learning methods used to analyze the large dataset generated in a Nano-TopoChip screening experiment allow us understand the relationship between nanotopography dimensions and shapes with the cell response. Many cell morphological parameters can be accurately predicted based on a few feature design parameters. With these methods we showed that size and spacing of the nanotopographies have a significant and reproducible effect on cell spreading. The nanotopographies cannot restrict the shape of the cells in contrast to the micro-scale topographies. This suggests that the nanotopographies must affect the availability and localization of cell attachment sites. Initially we hypothesized that this most likely occurs in an indirect manner, because unlike other studies that are able to restrict integrin binding domain availability by creating binding sites on a non-adhesive substrate (4), cells on the Nano-TopoChip are expected to able to bind on the non-patterned areas. The cell attachment there might be somewhat restricted because of the relatively high aspect ratio on small topographies with little spacing (200 nm width, 800 nm height), but otherwise the non-patterned areas have the same surface chemistry as the topographical features. Cells bind to serum ECM proteins, such a fibronectin, that adhere to the substrate material [32]. It is plausible that the nanotopographies influence the alignment of ECM proteins and perhaps the presentation of binding motifs such as RGD sequences. In this way, the nanotopographies may indirectly affect binding to cell adhesion molecules such as integrins which are transmembrane proteins that play a key role in cell-ECM interactions [33]. Clusters of integrins form the focal adhesion complexes that on the one side attach the cell to matrix proteins while on the other side anchor to the cytoskeleton through adaptor proteins such as talin, paxillin and focal adhesion kinase [34]. Even the smallest features are large enough to provide the surface area required for the formation of a small integrin cluster [4,35] required for focal adhesions. Nevertheless, the smallest nano features might limit the size of the integrin clusters. It is suggested that fewer, large integrin clusters result in less cell spreading and thick actin bundles while more, smaller integrin clusters with small spacing leads to more spread cells with smaller focal adhesion sites [36]. If the cells in our experiments preferably attach to the top of the topographical features, this would be consistent with our findings which show that fewer large features lead to adhered cells with rounded morphology whereas many small topographical features lead to spread cells.

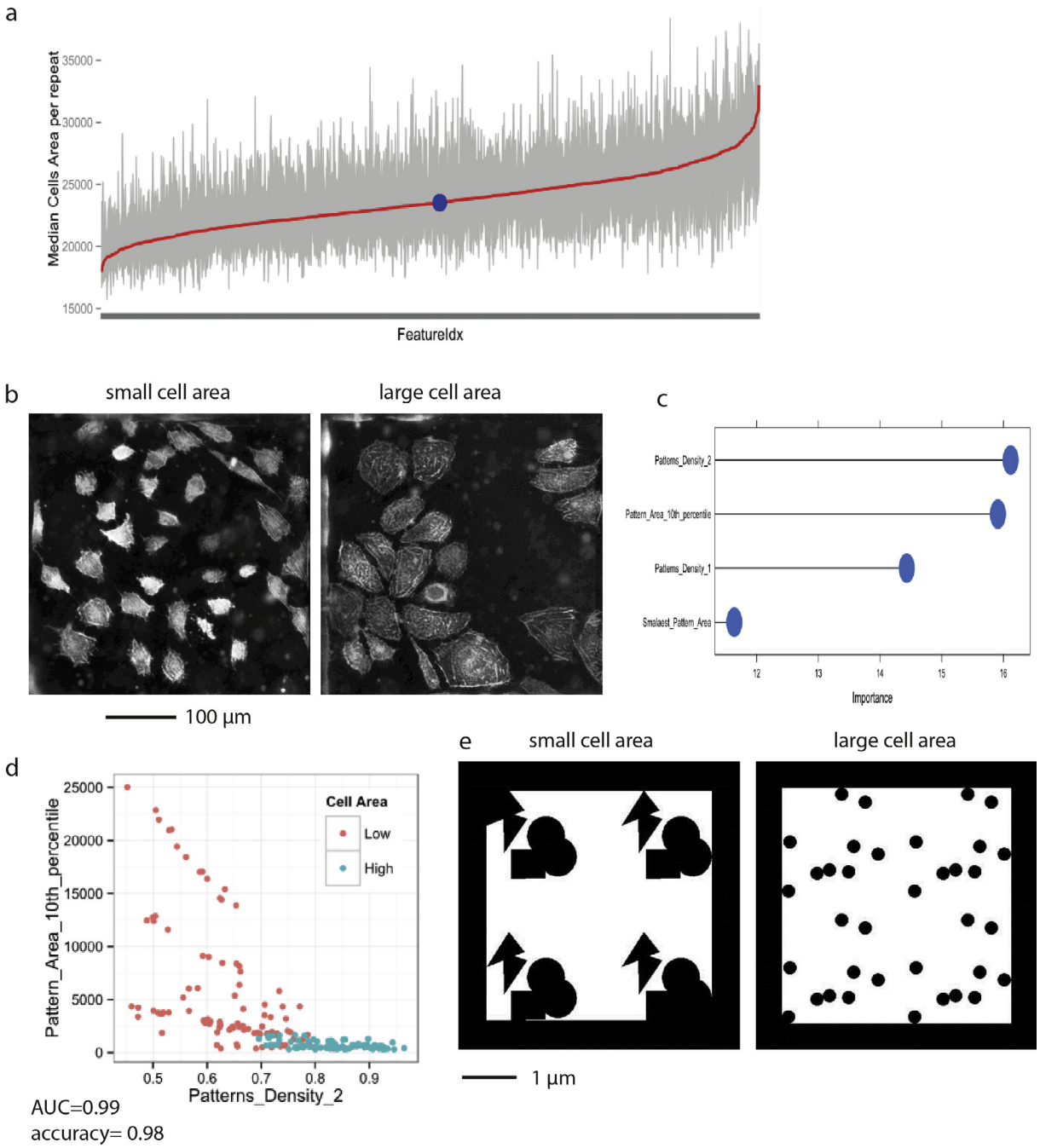

Fig. 5. Nanotopographies affect cell area. a: S-curve of Cell area measurement distribution. b: Representative images from the screening experiment which show U2OS with small and large cell areas. c: graph which shows the importance measurements of feature design parameters which influence cell area, by the random forest algorithm. An explanation of the Cell profiler features is presented in the Supplementary Table S2. d: Separation of cells with low and high cell area by the '10th percentile area' parameter and the 'pattern density' parameter. e: Representative images of features which influence cell area.

From our data we can conclude that the cell spreading is affected by the ratio of patterned versus non-patterned area. Although topographies with spread cells tend to have fewer cells this was not due to space limitation because the cell density in all images was confirmed to be sub confluent. It appears that the fully spread cells have a lower proliferation rate. The integrins in the focal adhesion complexes are mechanically connected to the nucleus through the actin cytoskeleton, and in this way can affect nuclear processes such as transcription and the cell cycle progression [37]. This data is quite preliminary. To verify possible effect of cell spreading on proliferation, one would need to perform more studies with lower initial cell seeding density and longer culture time.

In conclusion, this work showed the fabrication of the Nano-TopoChip, which contains a vast library of accurately defined, reproducible nanotopographies on biologically relevant surface areas. The flexibility of substrate material choice allows the identification of bioactive nanotopographies for many applications. Furthermore, a proof of principle screening experiment with U2OS cells demonstrated the Nano-TopoChip high-throughput screening platform as an excellent tool to investigate nanotopography – cell morphological parameter relationships. In future experiments the Nano-TopoChip can be used to identify specific nanotopographical designs, which influence functional cell phenotypes such as stem cell differentiation states.

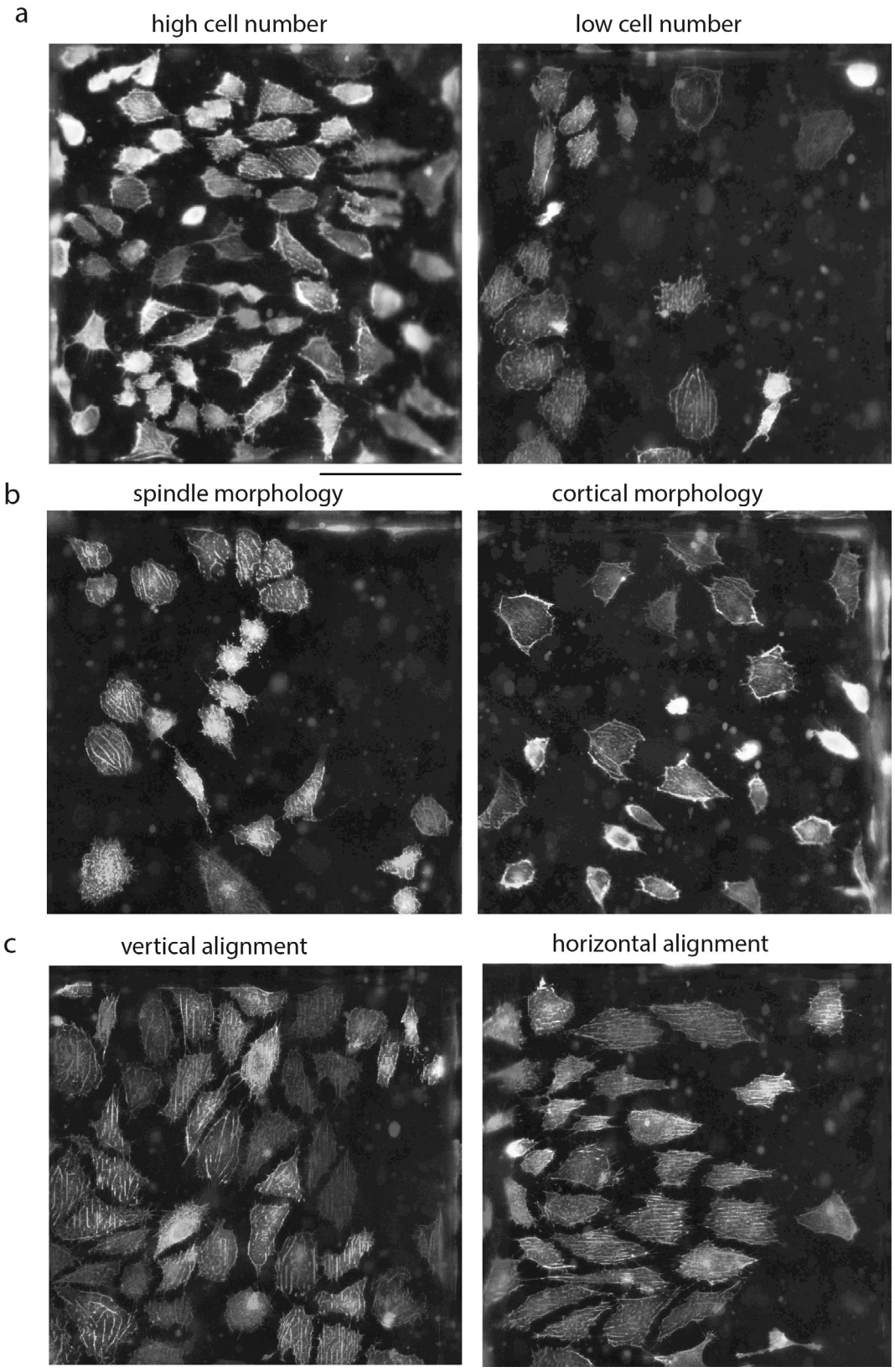

Fig. 6. Cell parameters which are affected by nanotopography. a: Representative images from the screen of TopoUnits with low and high cell number. b: Representative images from the screen of cells cortical actin localization and actin spindle morphology. c: Representative images from the screen of cells with vertical and horizontal actin fiber orientation. The scale bar has a length of 100 μm. The designs of the underlying topographies are shown in Suppl. Fig. 10.

Acknowledgements

JdB, DS and FH gratefully acknowledge the financial support of the NanoNext NL program 6c. JdB acknowledges the financial support of the Dutch province of Limburg, AV the European Union's Seventh Framework Program (FP7/2007-2013) (grant agreement 289720). DS acknowledges the financial support by the EU Marie Curie ITN Project BIOART (grant no.316690). FH thanks Mark Smithers from Mesa+ NanoLab for assistance with SEM. Materiomics BV acknowledges Jeroen Bolk, Robert Laar from *Nanolab@TU/e, Eindhoven University of Technology, Eindhoven, The Netherlands.*

Appendix A. Supplementary data

Supplementary data associated with this article can be found, in the online version, at http://dx.doi.org/10.1016/j.actbio.2017.08.023.

References

[1] A. Reimer, A. Vasilevich, F. Hulshof, P. Viswanathan, C.A. van Blitterswijk, J. de Boer, F.M. Watt, Scalable topographies to support proliferation and Oct4 expression by human induced pluripotent stem cells, Sci. Rep. 6 (2016) 18948. PubMed PMID: 26757610. Epub 2016/01/14. eng..

[2] M.L. Arlin, Survival and success of sandblasted, large-grit, acid-etched and titanium plasma-sprayed implants: a retrospective study, Journal (Canadian Dental Association) 73 (9) (2007) 821. PubMed PMID: 18028757. Epub 2007/11/22. eng..

[3] E. Makhija, D.S. Jokhun, G.V. Shivashankar, Nuclear deformability and telomere dynamics are regulated by cell geometric constraints, in: Proceedings of the National Academy of Sciences of the United States of America, 2016, pp. E32–E40. PubMed PMID: 26699462. Epub 2015/12/25. eng.

[4] M. Schvartzman, M. Palma, J. Sable, J. Abramson, X. Hu, M.P. Sheetz, S.J. Wind, Nanolithographic control of the spatial organization of cellular adhesion receptors at the single-molecule level, Nano Lett. 11 (3) (2011) 1306–1312. Pubmed Central PMCID: PMC3061283. Epub 2011/02/16. eng..

[5] E.A. Cavalcanti-Adam, T. Volberg, A. Micoulet, H. Kessler, B. Geiger, J.P. Spatz, Cell spreading and focal adhesion dynamics are regulated by spacing of integrin ligands, Biophys. J. 92 (8) (2007) 2964–2974. Pubmed Central PMCID: PMC1831685. Epub 2007/02/06. eng..

[6] W. Wang, L. Zhao, K. Wu, Q. Ma, S. Mei, P.K. Chu, Q. Wang, Y. Zhang, The role of integrin-linked kinase/beta-catenin pathway in the enhanced MG63 differentiation by micro/nano-textured topography, Biomaterials 34 (3) (2013) 631–640. PubMed PMID: 23107296. Epub 2012/10/31. eng..

[7] Q. Zhou, P.T. Kuhn, T. Huisman, E. Nieboer, C. van Zwol, T.G. van Kooten, P. van Rijn, Directional nanotopographic gradients: a high-throughput screening platform for cell contact guidance, Sci. Rep. 5 (2015) 16240. Pubmed Central PMCID: PMC4647116. Epub 2015/11/18. eng..

[8] K.A. Diehl, J.D. Foley, P.F. Nealey, C.J. Murphy, Nanoscale topography modulates corneal epithelial cell migration, J. Biomed. Mater. Res. Part A. 75 (3) (2005) 603–611. PubMed PMID: 16106433. Epub 2005/08/18. eng..

[9] J. Park, S. Bauer, K.A. Schlegel, F.W. Neukam, K. von der Mark, P. Schmuki, TiO2 nanotube surfaces: 15 nm – an optimal length scale of surface topography for cell adhesion and differentiation, Small (Weinheim an der Bergstrasse, Germany) 5 (6) (2009) 666–671. PubMed PMID: 19235196. Epub 2009/02/24. eng.

[10] G.M. de Peppo, H. Agheli, C. Karlsson, K. Ekstrom, H. Brisby, M. Lenneras, S. Gustafsson, P. Sjovall, E. Olsson, J. Lausmaa, P. Thomsen, S. Petronis, Osteogenic response of human mesenchymal stem cells to well-defined nanoscale topography in vitro, Int. J. Nanomed. 9 (2014) 2499–2515. Pubmed Central PMCID: PMC4039423. Epub 2014/06/07. eng.

[11] M.J. Dalby, N. Gadegaard, R. Tare, A. Andar, M.O. Riehle, P. Herzyk, C.D. Wilkinson, R.O. Oreffo, The control of human mesenchymal cell differentiation using nanoscale symmetry and disorder, Nat. Mater. 6 (12) (2007) 997–1003. PubMed PMID: 17891143. Epub 2007/09/25. eng.

[12] M. Yamada, E. Kato, A. Yamamoto, K. Sakurai, A titanium surface with nano-ordered spikes and pores enhances human dermal fibroblastic extracellular matrix production and integration of collagen fibers, Biomed. Mater. (Bristol, England) 11 (1) (2016) 015010. PubMed PMID: 26835848. Epub 2016/02/03. eng.

[13] S.P. Garland, C.T. McKee, Y.R. Chang, V.K. Raghunathan, P. Russell, C.J. Murphy, A cell culture substrate with biologically relevant size-scale topography and compliance of the basement membrane, Langmuir 30 (8) (2014) 2101–2108.

[14] G. Zhao, Z. Schwartz, M. Wieland, F. Rupp, J. Geis-Gerstorfer, D.L. Cochran, B.D. Boyan, High surface energy enhances cell response to titanium substrate microstructure, J. Biomed. Mater. Res. Part A 74 (1) (2005) 49–58. PubMed PMID: 15924300. Epub 2005/06/01. eng.

[15] S.E. Maclaine, N. Gadhari, R. Pugin, R.M. Meek, M. Liley, M.J. Dalby, Optimizing the osteogenicity of nanotopography using block co-polymer phase separation fabrication techniques, J. Orthopaedic Res. 30 (8) (2012) 1190–1197. PubMed PMID: 22294345. Epub 2012/02/02. Eng.

[16] K. Kolind, A. Dolatshahi-Pirouz, J. Lovmand, F.S. Pedersen, M. Foss, F. Besenbacher, A combinatorial screening of human fibroblast responses on micro-structured surfaces, Biomaterials 31 (35) (2010) 9182–9191. PubMed PMID: 20832853. Epub 2010/09/14. eng.

[17] A.A. Moe, M. Suryana, G. Marcy, S.K. Lim, S. Ankam, J.Z. Goh, J. Jin, B.K. Teo, J.B. Law, H.Y. Low, E.L. Goh, M.P. Sheetz, E.K. Yim, Microarray with micro- and nano-topographies enables identification of the optimal topography for directing the differentiation of primary murine neural progenitor cells, Small 8 (19) (2012) 3050–3061. PubMed PMID: 22807278. Epub 2012/07/19. eng.

[18] H.V. Unadkat, M. Hulsman, K. Cornelissen, B.J. Papenburg, R.K. Truckenmuller, A.E. Carpenter, M. Wessling, G.F. Post, M. Uetz, M.J. Reinders, D. Stamatialis, C. A. van Blitterswijk, J. de Boer, An algorithm-based topographical biomaterials library to instruct cell fate, Proc. Natl. Acad. Sci. U S.A. 108 (40) (2011) 16565–16570. Pubmed Central PMCID: 3189082. Epub 2011/09/29. eng.

[19] M. Hulsman, F. Hulshof, H. Unadkat, B.J. Papenburg, D.F. Stamatialis, R. Truckenmuller, C.A. van Blitterswijk, J. de Boer, M.J. Reinders, Analysis of high-throughput screening reveals the effect of surface topographies on cellular morphology, Acta Biomater. 15 (2015) 29–38. PubMed PMID: 25554402. Epub 2015/01/03. eng.

[20] W. Chen, Y. Shao, X. Li, G. Zhao, J. Fu, Nanotopographical Surfaces for Stem Cell Fate Control: Engineering Mechanobiology from the Bottom, Nano Today 9 (6) (2014) 759–784. PubMed PMID: 25883674. Pubmed Central PMCID: PMC4394389. Epub 2015/04/18. eng.

[21] A.E. Carpenter, T.R. Jones, M.R. Lamprecht, C. Clarke, I.H. Kang, O. Friman, D.A. Guertin, J.H. Chang, R.A. Lindquist, J. Moffat, P. Golland, D.M. Sabatini, Cell Profiler: image analysis software for identifying and quantifying cell phenotypes, Genome Biol. 7 (10) (2006) R100. PubMed PMID: 17076895. Pubmed Central PMCID: 1794559. Epub 2006/11/02. eng.

[22] R Development Core Team R: A Language and Environment for Statistical Computing.Vienna, Austria : the R Foundation for Statistical Computing, 2011. ISBN: 3-900051-07-0. Available online at http://www.R-project.org/.

[23] Y. Dodonov, DY, Distance-weighted statistics: robust estimation of location, spread and association between variables, 2013.

[24] M. Kuhn, Building Predictive Models in R Using the caret Package, 2008. 2008 2008-11-10;28(5):26. Epub 2008-09-23.

[25] M. Eichhorn, C. Stannard, K. Anselme, J. Ruhe, Nucleus deformation of SaOs-2 cells on rhombic micro-pillars, J. Mater. Sci. – Mater. Med. 26 (2) (2015) 108. PubMed PMID: 25665842. Epub 2015/02/11. eng.

[26] W. Li, Q.Y. Tang, A.D. Jadhav, A. Narang, W.X. Qian, P. Shi, S.W. Pang. Large-scale Topographical Screen for Investigation of Physical Neural-Guidance Cues. Sci. Rep. 2015, 03/02.

[27] R. Muhammad, G.S. Peh, K. Adnan, J.B. Law, J.S. Mehta, E.K. Yim, Micro- and nano-topography to enhance proliferation and sustain functional markers of donor-derived primary human corneal endothelial cells, Acta Biomater. 19 (2015) 138–148. PubMed PMID: 25796353. Epub 2015/03/23. eng.

[28] W.G. Brodbeck, Y. Nakayama, T. Matsuda, E. Colton, N.P. Ziats, J.M. Anderson, Biomaterial surface chemistry dictates adherent monocyte/macrophage cytokine expression in vitro, Cytokine 18 (6) (2002) 311–319. PubMed PMID: 12160519. Epub 2002/08/06. eng.

[29] S. Shadanbaz, G.J. Dias, Calcium phosphate coatings on magnesium alloys for biomedical applications: a review, Acta Biomater. 8 (1) (2012) 20–30. PubMed PMID: 12160519. Epub 2002/08/06. eng.

[30] Y. Mei, K. Saha, S.R. Bogatyrev, J. Yang, A.L. Hook, Z.I. Kalcioglu, S.W. Cho, M. Mitalipova, N. Pyzocha, F. Rojas, K.J. van Vliet, M.C. Davies, M.R. Alexander, R. Langer, R. Jaenisch, D.G. Anderson, Combinatorial development of biomaterials for clonal growth of human pluripotent stem cells, Nat. Mater. 9 (9) (2010 Sep) 768–778. Pubmed Central PMCID: PMC3388774. Epub 2010/08/24. eng.

[31] M.D. Treiser, E.H. Yang, S. Gordonov, D.M. Cohen, I.P. Androulakis, J. Kohn, C.S. Chen, P.V. Moghe, Cytoskeleton-based forecasting of stem cell lineage fates, Proc. Natl. Acad. Sci. U.S.A. 107 (2) (2010) 610–615. PubMed PMID: 20080726. Pubmed Central PMCID: PMC2818905. Epub 2010/01/19. Eng.

[32] A. Sethuraman, M. Han, R.S. Kane, G. Belfort, Effect of surface wettability on the adhesion of proteins, Langmuir 20 (18) (2004) 7779–7788. Pubmed Central PMCID: PMC2818905. Epub 2010/01/19. eng.

[33] M.A. Schwartz, M.H. Ginsberg, Networks and crosstalk: integrin signalling spreads, Nat. Cell Biol. 4 (4) (2002) E65–E68. PubMed PMID: 11944032. Epub 2002/04/11. eng.

[34] B. Geiger, J.P. Spatz, A.D. Bershadsky, Environmental sensing through focal adhesions, Nat. Rev. Mol. Cell Biol. 10 (1) (2009) 21–33. PubMed PMID: 19197329. Epub 2009/02/07. eng.

[35] L.Y. Koo, D.J. Irvine, A.M. Mayes, D.A. Lauffenburger, L.G. Griffith, Co-regulation of cell adhesion by nanoscale RGD organization and mechanical stimulus, J. Cell Sci. 115 (Pt 7) (2002) 1423–1433. PubMed PMID: 11896190. Epub 2002/03/16. eng.

[36] J. Huang, S.V. Grater, F. Corbellini, S. Rinck, E. Bock, R. Kemkemer, H. Kessler, J. Ding, J.P. Spatz, Impact of order and disorder in RGD nanopatterns on cell adhesion, Nano Lett. 9 (3) (2009) 1111–1116. PubMed PMID: 19206508. Pubmed Central PMCID: PMC2669488. Epub 2009/02/12. eng.

[37] A.J. Maniotis, C.S. Chen, D.E. Ingber, Demonstration of mechanical connections between integrins, cytoskeletal filaments, and nucleoplasm that stabilize nuclear structure, in: Proceedings of the National Academy of Sciences of the United States of America, 1997, pp. 849–854. PubMed PMID: 9023345. Pubmed Central PMCID: PMC19602. Epub 1997/02/04. eng.